

Flow topology in the wake of a cyclist and its effect on aerodynamic drag

T. N. Crouch^{1,†}, D. Burton¹, N. A. T. Brown², M. C. Thompson¹ and J. Sheridan¹

¹Fluids Laboratory for Aeronautical and Industrial Research (FLAIR), Department of Mechanical and Aerospace Engineering, Monash University, Clayton, VIC 3800, Australia

²Australian Institute of Sport, Belconnen, Canberra, 2617, Australia

(Received 3 June 2013; revised 1 October 2013; accepted 18 December 2013;
first published online 28 April 2014)

Three-dimensional flows around a full-scale cyclist mannequin were investigated experimentally to explain the large variations in aerodynamic drag that are measured as the legs are positioned around the 360° crank cycle. It is found that the dominant mechanism affecting drag is not the small variation in frontal surface area over the pedal stroke but rather due to large changes in the flow structure over the crank cycle. This is clearly shown by a series of detailed velocity field wake surveys and skin friction flow visualizations. Two characteristic flow regimes are identified, corresponding to symmetrical low-drag and asymmetrical high-drag regimes, in which the primary feature of the wake is shown to be a large trailing streamwise vortex pair, orientated asymmetrically in the centre plane of the mannequin. These primary flow structures in the wake are the dominant mechanism driving the variation in drag throughout the pedal stroke. Topological critical points have been identified on the suction surfaces of the mannequin's back and are discussed with velocity field measurements to elucidate the time-average flow topologies, showing the primary flow structures of the low- and high-drag flow regimes. The proposed flow topologies are then related to the measured surface pressures acting on the suction surface of the mannequin's back. These measurements show that most of the variation in drag is due to changes in the pressure distribution acting on the lower back, where the large-scale flow structures having the greatest impact on drag develop.

Key words: aerodynamics, wakes/jets

1. Introduction

Cycling aerodynamics is a particularly interesting subclass of bluff-body aerodynamics because of the wide variety of flows and fluid mechanisms that must be considered to properly manage the effects of aerodynamic drag. The need to better understand these flows in the context of competitive cycling is clear when the impact that aerodynamic forces have on cycling performance is considered. Whether it be elite track, road or endurance cycling, the difference between first and second place is highly dependent on the aerodynamic efficiency of cyclists and teams.

† Email address for correspondence: timothy.crouch@monash.edu

In some of the first experiments reported on cyclist aerodynamics, Kyle & Burke (1984) found that even for relatively low cycling velocities ($> 8.9 \text{ m s}^{-1}$) as much as 90% of the total resistance acting on a cyclist is attributable to aerodynamic drag. Other investigations into the power requirements of cyclists (Martin *et al.* 1998) have found that the aerodynamic drag component can account for as much as 96% of a cyclist's available power for cycling conditions at constant speed on a flat surface. Owing to the size and bluff-body nature of the geometry the majority of the drag is a result of the pressure drag that acts on the rider (Martin, Davidson & Pardyjak 2007). A review of a number of studies investigating the aerodynamics of cyclists over the past two decades by Lukes, Chin & Haake (2005), shows that reducing the projected frontal surface area by properly positioning the rider on the bicycle is an effective way to reduce the pressure drag. With the Union Cycliste Internationale (UCI) race rules placing restrictions on rider position, the extent to which further gains can be achieved through reduced frontal area is limited. This means that future gains must result from reductions in the drag coefficient.

Although there have been many investigations into the aerodynamics of cyclists, there is little literature discussing dominant fluid mechanisms and flow structures that have a large influence on a cyclist's drag. This is a reflection of both the competitive nature of cycling, where withholding research can provide teams with a competitive advantage, and also a current lack in understanding of the nature of the flow around cyclists. Currently the vast majority of research on the aerodynamics of cyclists has addressed the issue of aerodynamic drag from the perspective of the rider through measurement of the aerodynamic forces acting on the cyclist system. However, aerodynamic drag can also be assessed from the perspective of the fluid through which the cyclist moves, and measurement techniques that take this approach often provide much more information regarding how and where the drag force is generated. Wind tunnel studies have shown that aerodynamic drag is highly dependent on rider shape, size and position (Zdravkovich *et al.* 1996). Often athletes find it difficult to maintain positions during testing and for this reason, wind tunnel investigations have incorporated the use of cycling mannequins that can accurately define and maintain the geometries of a wide range of cyclist positions.

Currently, no picture of the gross wake structure or, more importantly, the large-scale flow structures, which have a significant impact on the aerodynamic drag force of a cyclist has yet emerged. Previous investigations into highly three-dimensional bluff-body flows, such as vehicle aerodynamics, have shown that investigating the wake structures can lead to a better understanding of how changes in vehicle geometry can affect the pressure distribution over the body, leading to changes in drag. In a review of road vehicle aerodynamics, Hucho & Sovran (1993) noted that one of the most influential findings in vehicle research and development has been the identification of large trailing streamwise vortices as a primary feature of vehicle wakes. Similarly by investigating the wake of cyclists and identifying wake structures that have the largest impact on the aerodynamic drag force, this will lead to a better understanding of how variations in rider shape and position will effect drag. It also follows that locating where the large separated regions occur on the body of the rider and knowledge of what the large-scale flow structures are would be extremely beneficial in the design of cycling equipment with the goal of minimizing the aerodynamic drag force acting on the rider.

In this paper we consider one of the fundamental aspects of cycling by investigating the effect that leg position has on drag. The insight gained from these studies has allowed us to determine the primary flow structure variants that have a large impact on

the drag force throughout the crank cycle. The evolution of the wake around the crank cycle has been analysed using a quasi-steady approach. For downhill riding conditions where cyclists usually do not pedal a quasi-steady assumption directly applies. For pedalling conditions a reduced frequency parameter ‘ k ’ can be calculated based on the ratio of the leg speed around the crank to the forwards riding velocity:

$$k = \frac{2r\pi f}{U_\infty}, \quad (1.1)$$

where U_∞ is the forward riding velocity, r is the crank length and f is the pedalling frequency in Hertz. For larger crank lengths (higher leg speeds for a given pedalling frequency) the reduced frequency parameter increases and unsteady effects should become more important. Figure 1 shows the range of reduced frequency values expected for various road and track cyclists under pedalling conditions. For elite cyclists where $0.08 < k < 0.18$ unsteady effects are likely to have some influence on aerodynamic forces. Currently the degree to which the pedalling motion will influence the aerodynamic forces and wake structures is still unknown. For some pedalling cadences under race conditions the reduced frequency parameter is not overly high and a quasi-steady approximation would be expected to account for the majority of the bulk fluid motion. Findings presented provide a sound starting point for the further development and understanding of unsteady aerodynamics associated with the motion of the legs whilst also providing a new perspective on how the aerodynamic drag force may be more efficiently reduced.

2. Experimental method

2.1. Wind tunnel experimental investigations

A range of quantitative and qualitative techniques were employed to investigate the effect that wake structures have on the time-averaged drag force throughout a pedal stroke. This includes wind tunnel measurements of aerodynamic drag forces, time-averaged wake surveys, skin friction flow visualization and time-averaged surface pressure measurements for varying leg positions. Experiments were conducted in two wind tunnels at Monash University: the Monash Large Wind Tunnel (MLWT) and the smaller Monash 450 kW Wind Tunnel (M450WT). Details of the two wind tunnels and turbulence and boundary-layer characteristics (test conditions) measured where the mannequin was positioned in centre of the test sections are shown in table 1. Measurements were performed at a typical road cycling velocity of 16 m s^{-1} which corresponds to a Reynolds number Re of 6.9×10^5 based on torso chord length. Aerodynamic forces and surface pressures were measured in the 3/4 open jet test section of the MLWT’s return circuit. Velocity field measurements and flow visualization studies were performed in the closed return circuit M450WT. The Reference pitot static tube measurements in the M450WT have been corrected for the effect of tunnel blockage by the method of Maskell (1963), which resulted in a 3.2% increase in the free-stream test velocity. To test that these findings were independent of the wind tunnel, a number of similar experiments were performed in each wind tunnel and compared. Surface pressure measurements on the back of the mannequin were repeated in the M450WT and show pressure distributions were not significantly affected by the higher blockage ratio in this wind tunnel. Variations in corrected pressure distributions averaged over all measurement points on the back for each leg position were $< 3\%$ between each wind tunnel.

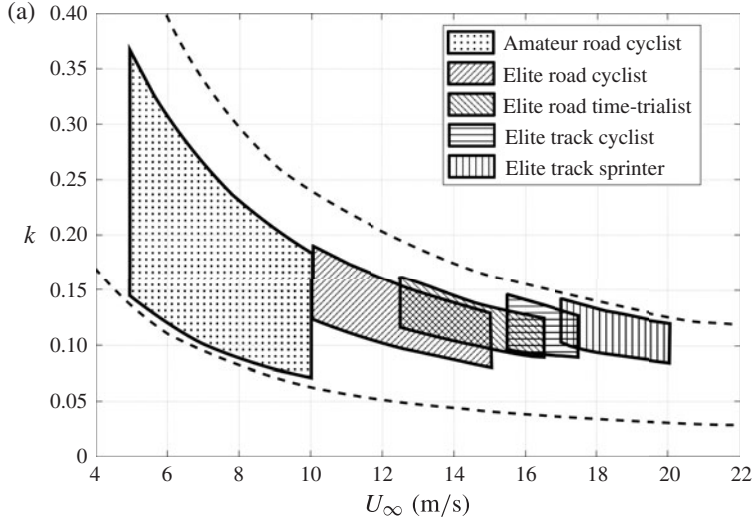


FIGURE 1. The range of the reduced frequency parameter calculated for various men’s and women’s road and track cycling events (based on typical cadences and crank lengths of each category). The area between the dashed lines covers the reduced frequency range for commercially available crank lengths 0.145–0.190 m and slow to high cadence frequencies 0.8–2.0 Hz.

Wind tunnel	MLWT	450 kW
Type	Return circuit open jet	Return circuit closed
Cross-sectional area	2.6 × 4.0 m (jet exit)	2.0 × 2.0 m
Test-section length	11.0 m	24.0 m
Turbulence intensity (mid-section)	< 1.6%	< 1.4%
Boundary-layer thickness (mid-section)	0.1 m	0.1 m
Blockage (mannequin)	≈ 4%	≈ 10%

TABLE 1. Comparison of main wind tunnel characteristics.

2.2. Cycling mannequin

As a result of the large effect that small variations in position can have on the aerodynamic forces, one of the major issues with athlete wind tunnel studies is the repeatability of rider position. In performing wind tunnel experiments on a mannequin, rider positions can be accurately repeated and maintained for extended periods of time and representative flow topologies can be developed and applied to human cyclists in order to reduce aerodynamic drag and improve performance. The Monash cycling mannequin was built in-house and approximates the physical dimensions of a male road cyclist whilst holding a standard time trial position. The design enables both the body geometry and the positioning of the limbs to be varied so that their effect on flow structures that impact drag could be investigated independently.

There are many parameters associated with the geometry, position and cycling equipment used that can have a significant impact on the aerodynamics of cyclists. Figure 2 shows a picture of the mannequin’s time trial position and the cycling equipment used. The position of the mannequin is representative of a low-drag

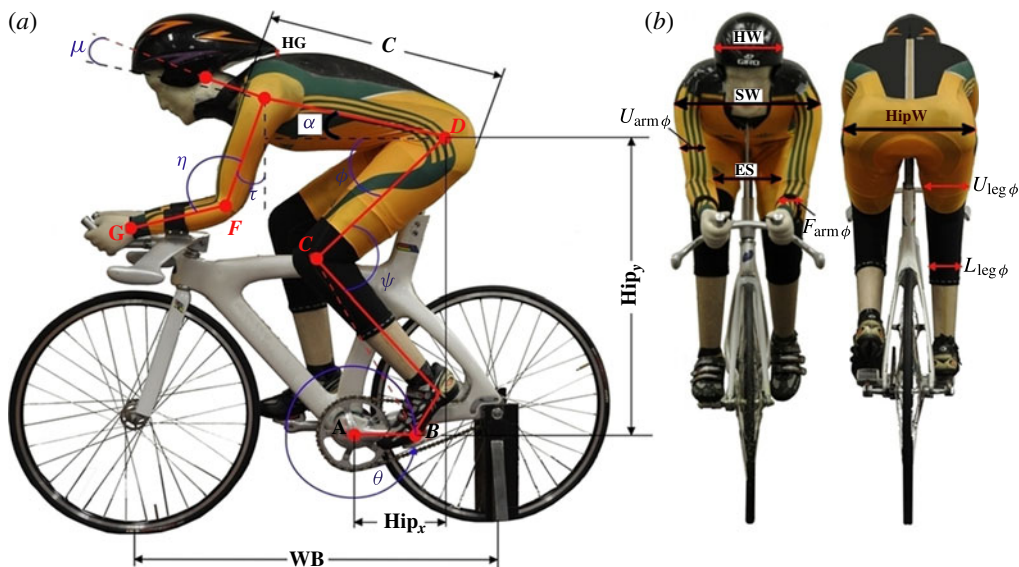


FIGURE 2. (Colour online) Mannequin position, equipment and major geometric properties.

position that is typically adopted during time trial stages of road races, triathlons and many track events. The helmet and skin suit are typical of those used by elite cyclists competing in these types of events. The bicycle is a Bike-Technologies track bike, size 54 cm frame with Mavic Open-Pro 32 spoke wheels. Figure 2 also depicts parameters that define the position and the main geometric properties of the mannequin which are listed in table 2.

The position of the mannequin's legs around the crank cycle is defined by the angle of the crank where the 0° crank position (shown in figure 2) occurs when the crank is horizontal, with the right leg forward and the left leg back. To simplify and constrain the dynamics of the legs, the ankle angle, which typically only varies $5\text{--}10^\circ$ throughout the pedal stroke, was locked in place at 90° inside the shoe. This constrained the motion of the upper-leg, lower-leg and crank in terms of a four bar linkage crank rocker mechanism.

2.3. Force measurements

Time-averaged aerodynamic forces were measured in the MLWT at 15° increments in leg position around a complete crank cycle. Forces acting on the mannequin and bicycle system were measured using a six-component Kistler force balance of the piezoelectric type that was calibrated prior to force measurements. The force balance consists of four individual three-component piezoelectric force transducers that are positioned in a horizontal quadratic arrangement to provide measurements of the three force and associated moment components. (For a more detailed description of Kistler-based (type 9067) force measurements relating to this type of arrangement refer to Cameron, Yarin & Foss (2007, Chapter 8).) Piezoelectric force transducers are of type 9067C and each has a maximum range, sensitivity and linearity of ± 30 kN, 8 pC N^{-1} and at most $\pm 0.25\%$ full-scale output (FSO), respectively. Quasi-static force data is acquired using a National Instruments PXI-1050 system (NI PXI-6284 card)

Name	Symbol	Position/length	Name	Symbol	Length (mm)
Crank angle	θ	0°:15°:360°	Foot-knee	B→C	558
Knee angle	ψ	$f(\theta)$	Upper leg	C→D	448
Hip angle	ϕ	$f(\theta)$	Torso	D→E	485
Angle of attack	α	12.5°	Upper arm	E→F	300
Upper-arm angle	τ	20°	Forearm	F→G	250
Elbow angle	η	110°	Neck	E→H	120
Neck angle	μ	5.0°	Helmet Width	HW	200
Head/helmet gap	HG	20 (mm)	Shoulder width	SW	420
Hip location (x)	Hip _x	200 (mm)	Elbow spacing	ES	160
Hip location (y)	Hip _y	806 (mm)	Hip Width	HW	350
Wheel base	WB	970 (mm)	Upper-arm diameter	$U_{arm\phi}$	80
Wheel diameter	W_ϕ	700 (mm)	Forearm diameter	$F_{arm\phi}$	72
Torso chord	c	640 (mm)	Upper-Leg Diameter	$U_{leg\phi}$	145
Crank	A→B	175 (mm)	Lower-leg diameter	$L_{leg\phi}$	90

TABLE 2. Characterization of mannequin position, size and shape.

through the force transducer platform and an eight-channel charge amplifier (Kistler type 9865b). The combined uncertainty associated with the force transducers and the data acquisition system is ± 0.565 N.

Struts attached to either side of the front and rear axles were used to rigidly fix the mannequin system to the force balance housed underneath the wind tunnel floor. The mannequin was positioned on a raised box with a cantilevered splitter extending over the leading edge of the platform to limit the impact of the raised box and the wind tunnel floor boundary layer on force results. Force measurements using the test set-up are taken as the mean result of three separate tests sampled at 500 Hz for 30 s at each crank angle. Each test involved recording baseline measurements with no wind before and after force measurements of the mannequin leg positions, meaning that any drift in force measurements over the duration of tests could be monitored and corrected. The maximum variation of force measurements at each position was less than 0.5% of the mean drag for all the leg positions tested.

2.4. Velocity field measurements

Detailed wake surveys of the time-averaged three-component velocity field vectors were performed in the M450WT for multiple streamwise planes orientated normal to the mean flow for varying leg positions. A two axis traverse was used to drive a four-hole dynamic pressure probe (Shepherd 1981; Hooper & Musgrove 1997), referred to herein as a probe, to multiple measurement locations within the streamwise traverse planes. The probe is capable of measuring velocities whose direction lies within $\pm 45^\circ$ of the probe axis (acceptance cone). The traverse consisted of a vertical axis that was rigidly fixed to the roof and floor of the wind tunnel that moved a horizontal axis which was mounted to it. A carbon fibre rod, which extended out from the horizontal axis, was used to hold the probe away from the traverse mechanism at a distance of at least 0.7 m, so that interference effects caused by the presence of the traverse in the flow at probe measurement locations were negligible. This was determined through experiment in free flow conditions as the point where the change in the free-stream velocity was less than 1%.

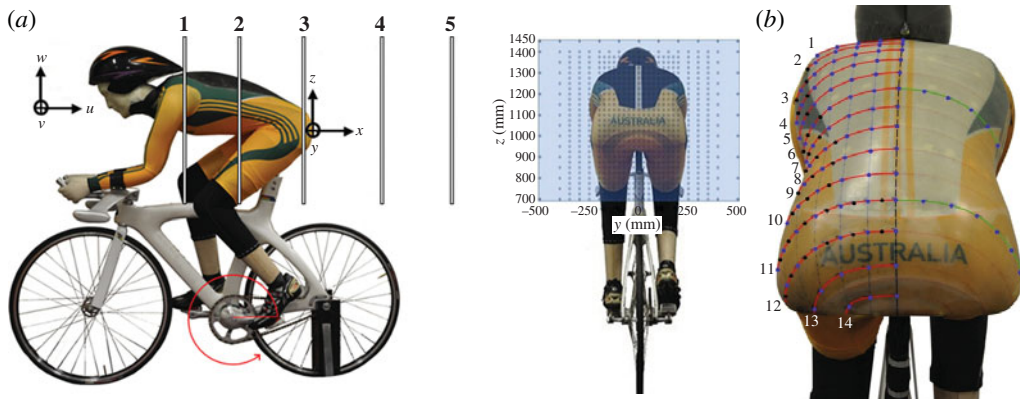


FIGURE 3. (Colour online) (a) Wake survey streamwise locations and traverse area. (b) Surface pressure measurement locations (taps) on the body of the mannequin.

Wake surveys captured the flow over the upper body and legs in a $0.75 \times 1.0 \text{ m}^2$ plane centred about the central plane of the mannequin 0.7 m above the wind tunnel floor. This particular section of the wake was chosen because it was found to contain the large-scale flow structures that have a significant impact on drag. Figure 3(a) shows the traversing area and the location of the five streamwise measurement planes. The location of each plane is referenced to the adopted coordinate system located at the trailing edge of the mannequin's lower back where symbols x , y and z denote the streamwise, spanwise and vertical coordinates. The three velocity components (u , v , w) associated with each of the coordinate system directions are also shown. The majority of sectional velocity field measurements were taken at traverse plane 5, which is located a torso chord length behind the trailing edge of the mannequin into the wake. For this plane wake surveys were performed for 15° increments around a complete crank cycle, corresponding to the leg positions where force measurements were obtained. For planes 1–4, located at the trailing edge of the helmet (1), mid-torso (2), hips (3) and half a torso chord length into the near wake (4), traverses were completed for selected leg positions representing flow regimes that were characteristic of high- and low-drag leg positions.

The wake surveys consist of probe measurements sampled at 1250 Hz for 15 s (18750 samples) at each measurement location in the traversing plane. The probe was traversed to capture the entire wake of the upper body with traverse measurements extending into the flow field that exhibited the same turbulence intensity as the free stream. Measurements were repeated at specific locations throughout traverses to ensure that mean flow measurements were repeatable. A second probe located in the free stream, 3.0 m upstream of the mannequin, was used as a reference. Reference probe measurements were recorded simultaneously throughout the duration of each traverse measurement and used to normalize any velocity or density variations resulting from changes in temperature and atmospheric pressure, over the duration of a traverse.

The spatial resolution of probe measurements made in the near wake (planes 4 and 5) of the mannequin was increased in areas of the wake that exhibited large velocity gradients. These areas were progressively refined throughout the traverse and were largely constrained to regions of the wake directly behind the mannequin. The final vertical and horizontal grid spacing between measurement points in this section

Plane	Location	No. of points	Mean cm ² /point	Leg positions
1	-3/4 C	1064	3.5	15°, 75°
2	-1/2 C	1125	3.8	15°, 75°
3	-1/16 C	1354	3.6	15°, 75°
4	1/2 C	924	8.1	15°, 75°
5	C	888	8.4	0°:15°:360°

TABLE 3. Total number of probe measurement points for each plane traversed.

of the wake was 25 and 20 mm, respectively. More grid points around the body of the mannequin were required to resolve the areas of the flow close to the surface. These regions exhibited large velocity gradients and required a greater number of total measurements to define the formation regions of flow structures developing over the back. In these areas the maximum vertical and horizontal grid spacing between measurement points was 10 and 20 mm, respectively, with measurements being refined to 5 mm from the surface in the vertical direction for the 20 mm closest to the surface. The number of measurements that fell outside the calibration limits of the $\pm 45^\circ$ acceptance cone of the probe was monitored carefully when investigating the wake of the mannequin. When measurements that fell outside these limits were omitted it had no observable effect on the final results. A breakdown of the total number of probe measurements made in each of the streamwise traverse planes is shown in table 3.

2.5. Surface pressure measurements

Surface pressures were measured in the MLWT for 15° increments in leg position around a complete crank cycle. Pressure taps were applied to the suction surfaces of the mannequin's back. As pressure tapping of the standard skin suit arrangement was not possible, a 4 mm fibreglass torso back section was developed that pressure taps could be fixed to. To create a flush join between the fibreglass shell and the skin suit fixed to the inside of the shell a silicon bead was applied around the edge.

To address the impact of the smooth fibreglass surface as opposed to the textured skin suit surface on the findings, force measurements were repeated for the range of leg positions tested, with the mannequin fitted with the fibreglass shell. Force results show that although mean forces were 7% higher for this arrangement, trends in the variation in drag were the same. With the mean force over the crank cycle subtracted, the variation in drag between the two mannequin test set-ups was less than 2%. The increase in drag is thought to result from the slight increase in projected frontal area of the addition of the 4 mm thick fibreglass shell and also the drag associated with the section of the network of tubing that was exposed to the flow during these measurements. Force results performed on a wide range of skin suits, where the surface roughness of the back section only was varied, has also been shown to have no significant effect on drag.

Two rack-mounted pressure modules from Turbulent Flow Instrumentation Pty Ltd (TFI), each with 64 individual pressure transducer channels, were used in parallel to measure mean surface pressures. Details of the pressure transducers used in each module are shown in table 4. A network of 125 polyvinyl chloride tubes of 1.2 mm internal diameter and 2.5 m in length connected the pressure taps on the surface of the mannequin to the pressure modules housed under the wind tunnel floor. Tubing runs

TFI module	A-1335	B-1336
Type	Differential	Differential
Number of channels	64	64
Pressure range	± 3 kPa	± 7 kPa
Accuracy	0.1% FSO	0.1% FSO

TABLE 4. Properties of the TFI surface pressure modules.

through the hollow fibreglass shell and then out behind the seat post, where tubes are positioned in the wake of the bicycle frame, and then down to the modules.

For each leg position, surface pressure measurements consisted of the average of three separate tests sampled at a rate of 500 Hz for 60 s. Time-averaged pressures varied less than 0.5% at each pressure measurement location between consecutive tests. All reported pressures are given as surface pressure coefficients that are referenced to the static pressure of the free stream at the test section centre. Reference pressures were measured by a pitot static tube placed 3.0 m in front of the test section centre. As a result of the variation in the static pressure distribution across the test section, typical of open jet wind tunnels (Mercker & Wiedemann 1996), reference pitot static tube measurements are corrected for their offset from the test section centre.

The location of pressure taps on the model is shown in figure 3(b). Pressure taps are located on the left half of the mannequin's back along lines that have been projected onto its surface, running perpendicular to the chord of the torso, labelled projection lines 1–14. By confirming a symmetrical pressure distribution across the centreline for opposite leg positions, the effective number of pressure tap locations can be doubled by tapping only one half the model and repeating surface pressure measurements for opposite leg positions. This assumption was checked by comparing surface pressures of symmetry taps located on the right-hand side of the body. The variation in time-averaged pressures between pressure taps and their symmetrical counterpart located on the right-hand side of the back was less than 5% for all taps and all leg positions. Projection lines are evenly spaced on the surface at 20 mm intervals along the centreline and begin at the tip of the trailing edge of the helmet finishing at the base of the lower back. By distributing taps along these lines a gridded arrangement of taps is generated on the three-dimensional curved surface of the mannequin's back. The optimal distribution of taps along each projection line was found by redistributing taps to areas where large pressure gradients existed.

2.6. Flow visualizations

Prior to the fibreglass torso back section being pressure tapped the oil flow method described by Maltby (1962) and the ink dot method similar to that developed by Langston & Boyle (1982) were used to visualize the time-averaged skin-friction distribution on the suction surfaces of the back. The oil was a mixture of kerosene, China clay and fluorescent paint and was applied using a pressurized spray gun. The ink dot method used a mixture of black water-based paint and water that was applied to the surface using a fine paint brush. A 'piecemeal' approach was then adopted where small regions of the back were investigated at different times to build a larger picture of skin friction patterns. Photographs were taken of the resulting skin friction patterns and were analysed using kinematical principles and critical point theories (Peake & Tobak 1982; Hornung & Perry 1984) to identify separation lines,

attachment lines and critical points where the wall shear stress is zero. Coupled with the wake surveys performed over the body of the mannequin and the surface pressure measurements, these flow visualizations provide further evidence to the structure of the complicated near-wake flow topology for different leg positions.

As the torso is highly three-dimensional, skin friction patterns are a result of both gravity and the air flow near the surface. To achieve clear images of flow visualizations and to minimize the effect of gravity, experiments were performed at a higher wind tunnel speed of 25 m s^{-1} , equivalent to $Re = 10.8 \times 10^5$ based on torso chord, so that the oil and paint flow was primarily a result of the wall shear stress and not gravity. Surface pressures on the back and wool tuft flow visualizations were repeated at the higher test speed and showed that the increase in Reynolds number had no observable effect on the pressure distribution and flow separation/reattachment locations. Results from oil visualizations are compared with the ink dot method, which used a more viscous fluid and consequently its motion on the surface was less affected by gravity. Both methods are in very good agreement with each other and multiple tests performed for similar leg positions showed visualizations are repeatable. The effect of gravity was further minimized by applying the oil and paint to the surface while the wind tunnel was running at low speed, this reduced the time required to reach operational test speed.

3. Results and discussion

3.1. *Effect of crank angle on drag*

We first consider the effect of leg position around the crank on the time-averaged drag force (D) acting on the mannequin. Figure 4(a) shows how the drag force, represented by the drag area $C_D A = D / (1/2 \rho U_\infty^2)$ (where ρ is the air density), varies as the legs are positioned around the crank cycle. The drag area varies significantly throughout the pedal stroke with a 20% variation in drag over both halves of the crank cycle.

The results for the two halves of the crank cycle are in reasonable agreement indicating good model symmetry, with a maximum variation in drag of opposite leg positions being less than 5%. Both halves show the drag does not change significantly over the first 15° of rotation, after which it increases rapidly for the next 60° , where it reaches a maximum at the 75° and 255° leg positions. Following the peak in drag in both halves of the crank cycle the drag decreases at a reduced rate compared with the rate at which it increased. It can be seen that over the range of crank angles where the drag reduces, a more rapid reduction in drag occurs during the second half of the crank cycle. The traverse results and surface pressure measurements completed around a complete crank cycle, suggest that this difference can be attributed to small asymmetries in the geometry and positioning of the mannequin. These minor differences between opposite leg positions do not compromise the overall conclusions drawn and we assume one half of the crank cycle to be representative of the data trend.

The change in the drag area with crank angle can be explained by a variation in the frontal area, a change in the drag coefficient or a combination of both. In an initial attempt to explain the change in drag throughout the crank cycle the combined frontal area of the bicycle and mannequin system (A) was determined for each leg position and is compared with the drag in figure 4(a). The projected frontal area was determined from photographs taken from 10 m in front of the mannequin, with a reference area held at the midpoint of the crank. The frontal area was then determined by counting pixels that lay within the boundaries of the bicycle and mannequin. The

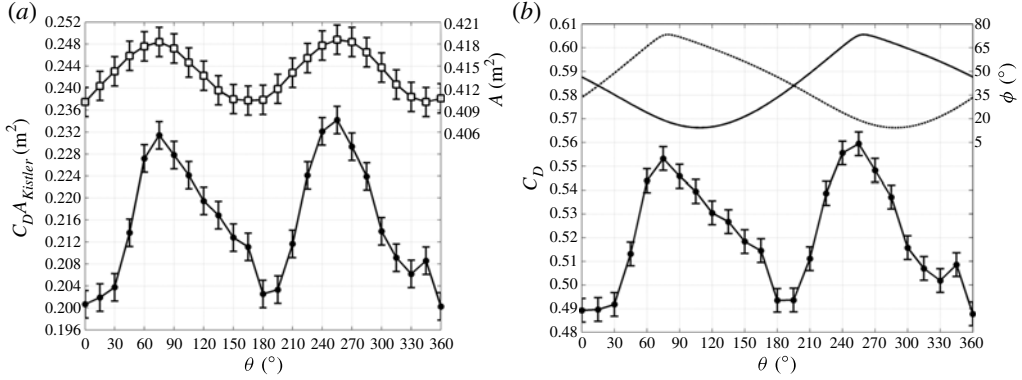


FIGURE 4. Variation in (a) drag area (—●—, left-hand axis) and projected frontal area (—□—, right-hand axis) and (b) drag coefficient (—●—, left-hand axis) and left (—) and right (···) leg hip angles (right-hand axis) with crank angle.

small change in frontal area which varies less than 2% over the crank cycle does not account for the large variations in drag, despite the frontal area maxima and minima coinciding with the low- and high-drag crank positions. Figure 4(b) shows that when the variation in frontal area on drag is taken into account and extracted out of the drag area values, the drag coefficient, defined by $C_D = D/(1/2\rho U_\infty^2 A)$, is primarily responsible for the variations in drag. Trends in the drag coefficient are similar to drag area, which varies up to 15% with leg position. Interestingly figure 4(b) also shows that the minimum in the drag coefficient coincides with crank angles when the upper thighs of both legs are closely aligned ($\phi_{\text{Left}} = \phi_{\text{Right}}$) and the maximum occurs when one of the legs is at its most extended position corresponding to when the hip angle of that leg is at a maximum ($\max(\phi_{\text{Left}}), \max(\phi_{\text{Right}})$).

3.2. Classification of characteristic flow regimes

The large variation in the drag coefficient suggests that as the legs move around the crank there is a large change in the flow regime around the mannequin. Figure 5 shows time-averaged contours of the out-of-plane non-dimensional streamwise velocity component and the principal turbulence intensity defined by $\sqrt{1/3(u'^2 + v'^2 + w'^2)}/U_\infty$ for the wake traverses performed at plane 5, a torso chord length behind the mannequin. As findings from traverse results are essentially the same for both halves of the crank cycle wake surveys are only shown for the first half of the crank cycle, which shows large variations in the size and shape of the wake as the crank cycle progresses. It is clear that the effect of leg position on the structure of the wake is not constrained to regions near the legs where movement occurs, but the entirety of the upper wake is affected.

Contours of streamwise velocity and principal turbulence intensity identify two prominent flow regimes in each half of the crank cycle. For the 15° and 195° low drag leg positions, where the upper thighs are aligned ($\phi_{\text{Left}} = \phi_{\text{Right}}$), the wake is symmetrical about the centre plane of the mannequin. As the legs are moved around each half of the crank cycle the wake progressively undergoes a transition to an asymmetrical flow regime. Once this has occurred the defining features of this regime remain relatively stable and we define the high drag 75° and 255° leg positions as being representative of the asymmetrical flow regime in each half of the crank cycle.

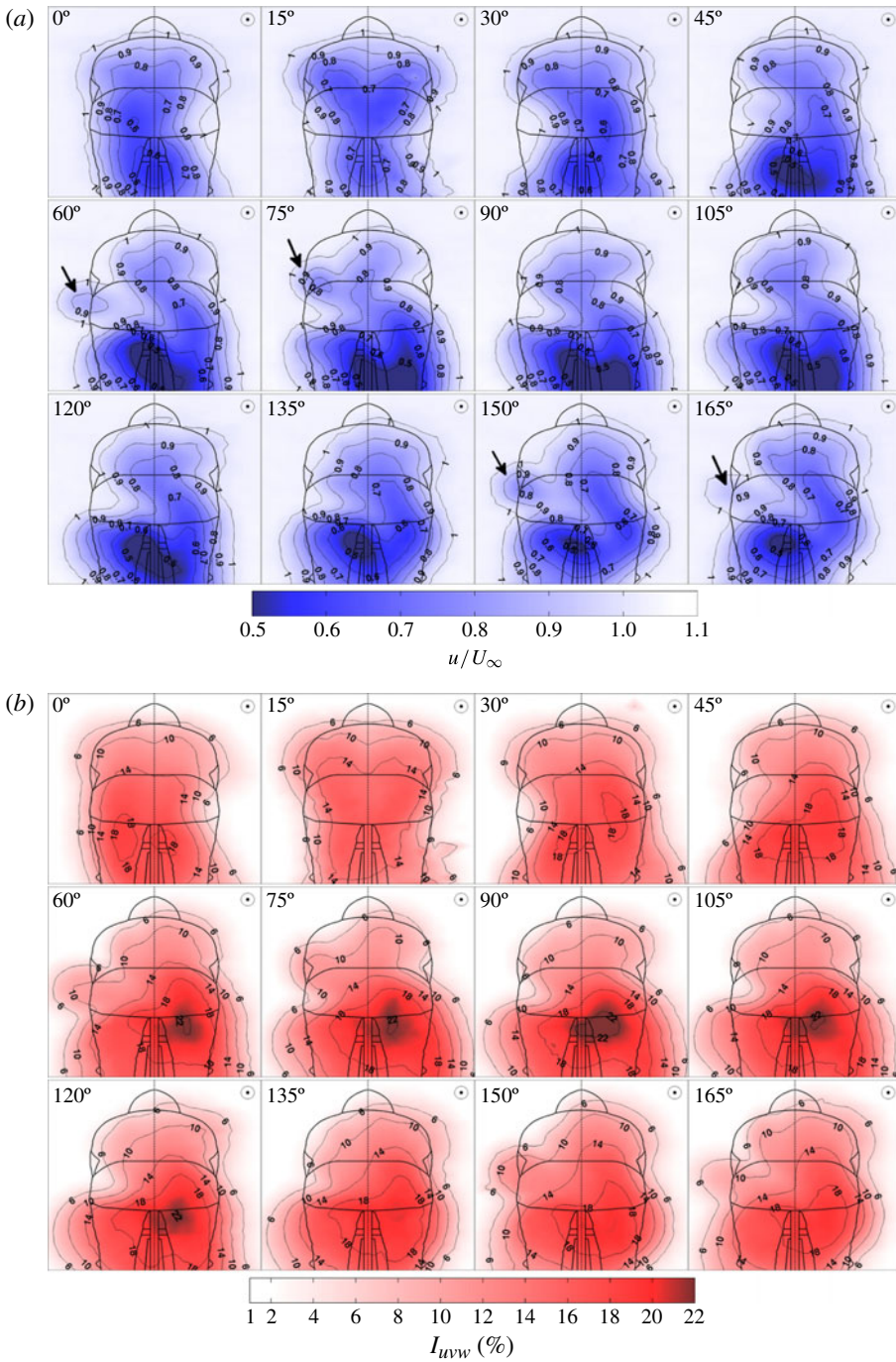


FIGURE 5. (Colour online) (a) Contours of the streamwise velocity component with isolines drawn for varying leg positions. Arrows highlight the isolated section of the wake that develops downstream of the arm/elbow joint during the asymmetrical flow regime. (b) Contours of principal turbulence intensity with isolines drawn for varying leg positions.

The majority of the variation in the wake, and consequently the drag force, throughout the crank cycle is a result of the low-velocity turbulent regions of the wake that develop below the hips. The difference in the two regimes is primarily a result of a variation in the location at which flow separates from the hips and lower back. For the symmetrical flow regime, the flow separates evenly across the lower back resulting in the increase in the size of the wake above the hips. The asymmetries in the flow for the high-drag flow regime develop due to a variation in the location at which the flow separates from the left and right sides of the hips and lower back. During the asymmetrical regime, flow remains largely attached over the side of the torso and hips where the leg is in a raised position, resulting in relatively high streamwise velocity and low turbulence in the wake downstream of this side of the torso. As the flow separates low on the rear base of the hip of the raised leg, large velocity defects and high turbulence levels are found below the hips. On the opposite side of the body, where the leg is extended, flow separates much earlier and higher on the hip resulting in an increase in the size of the wake above them.

It is also evident that the position of the legs significantly affects the location at which flow separates from other regions of the body. For crank angles 60–75° and 150–165° in the first half of the crank cycle, figure 5 shows a turbulent low-velocity separated region that develops near the outer left hip, which is highlighted by the arrows in the contours of streamwise velocity. In the first half of the crank cycle this separated region, which is later found to develop from the arm/elbow, is initially isolated from the main body of the wake. As the legs move further into the crank cycle this area of the wake then progresses towards the centre plane of the mannequin and joins the main wake body, finally receding out towards the outer left hip.

3.3. Identification of large-scale wake structures

Contours of the out-of-plane streamwise vorticity component in figure 6 show that the time-averaged flow exhibits large-scale streamwise vortices whose formation, strength and interaction depend on leg position. These structures constitute the major separated flow regions in the wake of the mannequin and, as a result, have a large effect on the drag throughout the pedal stroke. Similar to the characteristic flow regimes described previously, contours of streamwise vorticity exhibit a low-vorticity, low-drag symmetrical profile and an asymmetrical high-drag profile where the large separated regions of the wake are characterized by regions of high streamwise vorticity.

From the two-dimensional sectional velocity data streamwise vortices have been identified in figure 6 using the swirling strength criterion formulated by Zhou *et al.* (1999). Like other dimensionally equivalent vortex identification schemes that been shown to identify coherent vortex structures within shear flow regions (*Q criterion* and *λ_2 criterion*) this Galilean invariant method is based on the velocity gradient tensor

$$\nabla \mathbf{u} = \begin{bmatrix} \frac{\partial v}{\partial y} & \frac{\partial v}{\partial z} \\ \frac{\partial w}{\partial y} & \frac{\partial w}{\partial z} \end{bmatrix}. \quad (3.1)$$

The velocity gradient tensor has a complex conjugate eigenpair ($\lambda_{cr} \pm i\lambda_{ci}$) when the discriminant of the characteristic equation of $\nabla \mathbf{u}$ is less than zero. Zhou *et al.* (1999) determined that vortices correspond to regions where the imaginary component of the complex eigenvalues is greater than zero, $\lambda_{ci} > 0$. To improve the signal-to-noise

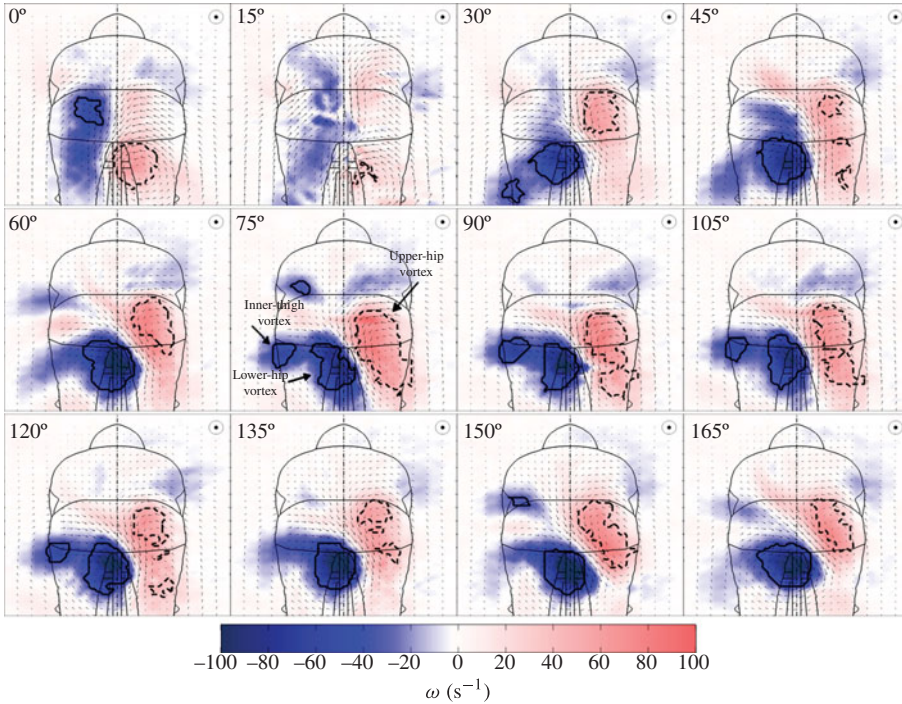


FIGURE 6. (Colour online) Contours of streamwise vorticity with vortex boundaries delineated by the swirling strength criterion. Solid lines outline vortex structures of clockwise rotation and dashed lines show vortices of anti-clockwise rotation. Primary wake vortices have been labelled for the high-drag 75° leg position.

ratio the imaginary part of the complex eigenvalue is typically squared λ_{ci}^2 and is used as a threshold to identify vortices (Carmer *et al.* 2008). Threshold levels help to differentiate between turbulent structures that exist within the free-stream flow and measurement noise. Background levels of λ_{ci} are found from measurements taken in the free stream (wind tunnel traverse without the mannequin). In this case, as λ_{ci}^2 has been used to identify vortices, the threshold level was set as the square of the maximum level of the swirling strength in the time-averaged free-stream velocity field $\lambda_{max\infty}^2$. Areas of $\lambda_{ci}^2 > \lambda_{max\infty}^2$ in the wake are identified as vortex structures that are not related to the free-stream flow and result from vorticity being generated at the surfaces of the mannequin.

The swirling strength criterion clearly identifies a large pair of counter-rotating streamwise vortices in figure 6 as the primary feature of the wake flow for the majority of leg positions in the high-drag asymmetrical flow regime. Please also see the supplementary movies available at <http://dx.doi.org/10.1017/jfm.2013.678>. For the low-drag regime in each half of the crank cycle, large coherent streamwise vortices are not present a torso length behind the mannequin. As the legs move around the crank and the flow transitions to the asymmetrical high-drag regime, a large streamwise vortex pair forms. This vortex pair is orientated asymmetrically across the centre plane of the mannequin. A topological analysis of the near-body flow presented in §3.5 shows that these vortices result from vorticity that is fed into the wake as vortex sheets that roll up from flow that separates from:

- (a) low on the base of the hip that is in a raised position, generating the vortex structure that is positioned lower in the wake (lower-hip vortex);
- (b) the upper hip and side of the torso where the leg is in an extended position, generating the second vortex that is orientated higher in the wake (upper-hip vortex).

To gain a clearer picture of the transition process throughout the full crank cycle, figure 7 shows the spatial development of vortices in traverse plane five for the different leg positions. This is represented as isosurfaces drawn from different perspectives of regions of high vorticity within the boundaries of vortex regions identified using the swirling strength criterion. The location of primary streamwise vortices originating from each side of the body alternates between a low position in the wake, when the leg is raised, and a higher position in the wake, when the leg is extended. The asymmetry in the location of flow separation results in the main vortex pair being skewed in both the vertical and horizontal directions of the wake. The lower of the pair is located close to the centre plane and the higher of the pair positioned further out. This orientation results in the flow being strongly yawed across the hip in the raised position and the downwash generated between the vortex pair being directed across the centre plane of the mannequin.

Another noticeable feature of the wake flow is a smaller streamwise vortex positioned below the outer hip of the raised leg, this can also be seen in figures 6 and 7. This vortex originates when flow separates from the inner thigh of the raised leg. The formation of this vortex is similar to that visualized by Ramberg (1983) for vortices that form at the upstream ends of inclined finite cylinders. Although similarities can be drawn between experiments performed on inclined cylinders, the presence of the torso and the opposite leg in the extended position have a large effect on the formation of streamwise vortices originating from the inner thigh of the raised leg, which is discussed in § 3.5.1.

3.4. Analysis of primary wake structures

By analysing the wake and its constituent vortex structures identified in figure 7, the effect of leg position on the strength, merging and drag contribution of vortex structures is determined. We first consider the contribution of the drag from primary vortex structures by performing a wake integral analysis developed by Maskell (1973) on the traverse planes discussed thus far. This method is an application of the momentum equation applied to a control volume that contains the model. The drag area can be calculated from the detailed wake surveys using (3.2) that takes into account defects in wake stagnation pressure, streamwise velocity and the drag contribution of the in-plane velocity components (Hucho & Sovran 1993):

$$C_{DA} = \iint_A \frac{P_{r\infty} - P_t}{\frac{1}{2}\rho U_\infty^2} da + \iint_A 1 - \left(\frac{u}{U_\infty}\right)^2 da + \iint_A \left(\frac{v}{U_\infty}\right)^2 + \left(\frac{w}{U_\infty}\right)^2 da, \quad (3.2)$$

where $P_{r\infty}$ and P_t are the static pressure of the free stream and the total pressure measured in the wake, respectively.

Figure 8(a) compares the wake integral approach applied to the wake traverses taken a torso chord length into the wake ($C_{DA_{Wake}}$) with the drag force measured using the force balance ($C_{DA_{Kistler}}$). As expected, forces calculated using this method are approximately 25% lower than the measured force results, mainly due to (3.2) being applied to only a partial section of the wake. Although absolute values cannot be

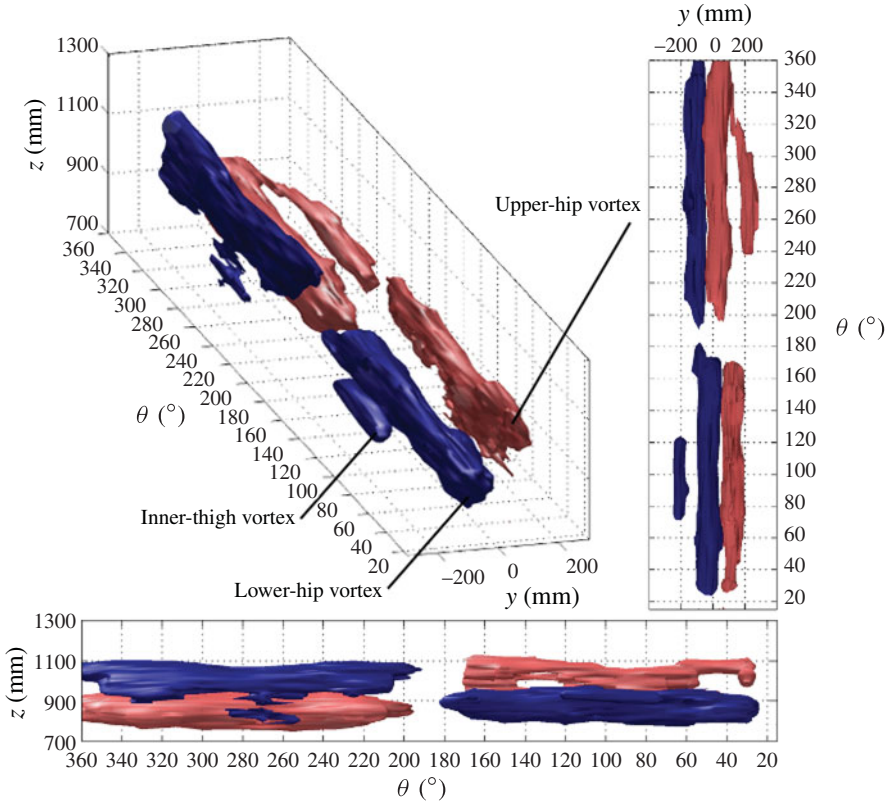


FIGURE 7. (Colour online) Primary vortex structures in the wake of the mannequin for varying leg positions. Vortex structures are visualized from different perspectives using surfaces of the swirling strength criterion throughout the crank cycle. Structures are coloured by streamwise vorticity, where dark (shown in blue online) and light (shown in red online) colours represent clockwise and anti-clockwise rotation, respectively.

compared directly, the variation in drag over the crank cycle for both force results is consistent. The minor asymmetries in force measurements across both halves of the crank cycle are also reflected in the wake integral analysis, providing further evidence of consistent results across both of the wind tunnels used in this investigation.

The agreement between the drag results also suggests that the most important features of the wake causing variations in the drag with leg position have been captured in the upper section of the traverse plane. This can be seen in figure 8(a) that also shows the contribution to the drag from vortex structures ($C_{DA_{Vortex}}$) identified in figure 6, calculated by applying (3.2) to areas of the wake within vortex boundaries. Although the primary vortex structures in the asymmetrical flow regime only account for 20–30% of the total drag approximated by integrating the entire traverse plane, when present in the traverse plane they account for almost all of the variation in drag over the crank cycle. Drag associated with streamwise vortices increases rapidly from when they first appear in the traverse plane until they peak at the high-drag 75° and 255° leg positions. Following this peak, similar to the drag measured with the force balance, their drag decreases. We also see a second peak in the drag associated with streamwise vortices at the 150° and the opposite 330° leg positions. These correspond

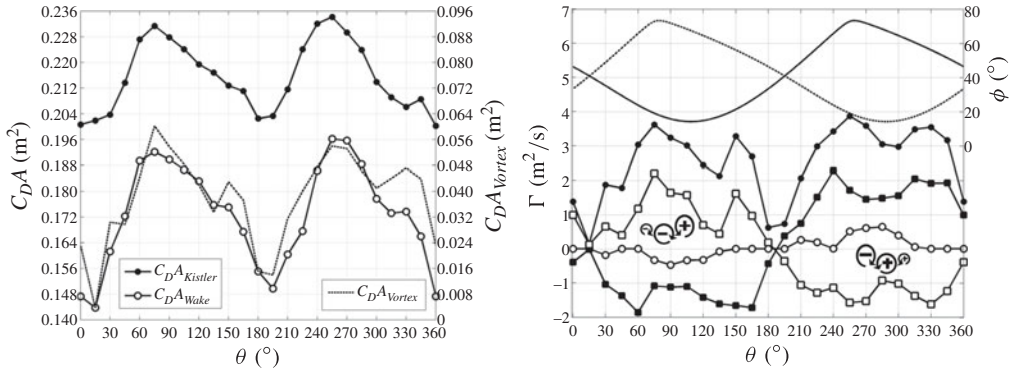


FIGURE 8. (a) Comparison of integrated wake and vortex drag approximations with drag measured using the Kistler force balance. Note both axes are of the same scale. (b) Breakdown of circulation of primary vortex structures: (—■—) primary lower-hip vortex; (—□—) primary upper-hip vortex; (—○—) inner-thigh vortex; (—●—) total sum of the absolute value of circulation from each vortex. Left (—) and right (···) hip angles are plotted on the right-hand axis.

to the leg positions where we observe a ‘kink’ in the total drag in each half of the crank cycle.

The large variation in drag that results from streamwise vortices indicates that leg position not only dictates the flow regime but also the relative strength of wake structures. To quantify the effect of leg position on the strength of primary streamwise vortices, their circulation over the course of the pedal stroke has been calculated. Figure 8(b) shows the circulation of streamwise vortices that comprise the main vortex pair and also the smaller inner-thigh vortex throughout the crank cycle. The circulation of each vortex was determined by evaluating the surface integral of the streamwise vorticity field within vortex boundaries determined by the swirling strength criterion $\Gamma_i = \int_A \omega_x da$. The total circulation was found by summing the absolute value of the circulation from each vortex $\Gamma_{total} = \sum_n |\Gamma_i|$.

Despite minor asymmetries, the major trends in the circulation of each of the structures analysed is consistent in both halves of the crank cycle. We see the circulation from the lower-hip vortex during the asymmetrical flow regime in both halves of the crank cycle peak (– and +) at the 60° and opposite 240° leg positions, after which the circulation first decreases and then increases again until the 165 and 345° leg positions. Interestingly, over the crank angles at which the inner-thigh vortex is identified in the traverse plane, an increase in the circulation of this vortex is associated with a decrease in the circulation of the lower-hip vortex, and vice versa. When the circulation associated with these two vortices of the same sign are summed the value remains relatively constant over leg positions 60–165° in the first half of the crank cycle and 240–345° in the second half suggesting strong interaction between the two. Owing to the close proximity at which these two structures form and the nature of vorticity generation on bodies, it is not surprising that they influence one another. Merging of these two vortices is also evident in figures 6 and 7, particularly in the second half of the crank cycle.

The circulation from the upper-hip vortex also varies throughout the crank cycle in a similar manner to the lower-hip vortex, with two key differences. First, the initial peak occurs later in the crank cycle at the high-drag 75 and 255° leg positions when

the hip angle is at a maximum. Second, following a decrease in circulation, a clear second peak in the circulation of this vortex can be seen at the 150° and opposite 330° leg positions. Interestingly these two peaks in each half of the crank cycle (first, 75° and 150° ; second, 255° and 330°) occur at approximately the same 20° hip angle of the opposite leg to where this vortex forms. This suggests that the position of both legs affects the formation and strength of the primary vortex structures on both sides of the wake. This is expected given that the torso, where these structures originate, is of a low aspect ratio (0.55 torso-chord-to-hip-width ratio).

The vortex drag, which accounts for the majority of the variation in the drag over the crank cycle, is highly dependent on the relative strength of each of these vortex structures which is shown to be closely related to where the leg is positioned around the crank cycle. When we take into account the total sum of the circulation of the primary vortex pair and the inner-thigh vortex, and compare it with the vortex drag shown in figure 8(a), it is clear the vortex drag varies with the strength of these vortices in the wake.

3.5. *Development of characteristic flow topologies*

The flow topology depicting the origin and formation mechanisms of primary vortex structures around a rider is important to visualize for a number of reasons. First, surface pressures which dictate the aerodynamic forces and contribute the greatest proportion to the total resistance are highly dependent on the local flow conditions near the surface of the rider, where large-scale flow structures develop. Second, the location of the large separated formation regions of the primary flow structures can isolate specific areas on the body where the greatest drag savings can be achieved. An understanding of both the location and flow mechanisms which describe where and how the large-scale flow structures develop will lead to informed and more efficient decisions on how better to minimize the effects of aerodynamic drag. Whether this be through the manipulation of both rider and cycling equipment geometry/position or the addition of other passive flow control mechanisms using known techniques in targeted areas to affect the formation and development of the large scale flow structures that have the greatest impact on drag.

As is commonly the case with complex turbulent three dimensional separated flows, a variety of techniques were required to deduce the overall structure of the flow. Investigations of flow structures that develop over the body of the mannequin involved both the additional streamwise traverses (planes 1–4) and skin friction flow visualizations. These results are discussed in relation to the 15° low-drag symmetrical and 75° high-drag asymmetrical flow regimes to deduce the effect leg position has on the time-averaged characteristic flow topologies. As a result of the ‘fragmented’ nature of the results used to piece together the overall flow structure, a general picture of the flow topology for each flow regime aids in the interpretation of results presented in the following section. Figure 9 shows the proposed flow topology for the 15° low-drag symmetrical and 75° high-drag asymmetrical flow regimes. The schematic highlights the identification of several additional streamwise vortices for each of the characteristic flow regimes and the location of major separation lines and critical points from which streamwise vortices originate.

In providing evidence to support the proposed flow topologies depicted in figure 9, the multiple streamwise vortices are first identified from the additional streamwise traverses. These are then discussed in relation to the time-averaged skin friction flow visualizations, which locate the origin of the large-scale flow structures on the body of the mannequin. Time-averaged large-scale and smaller secondary flow structures

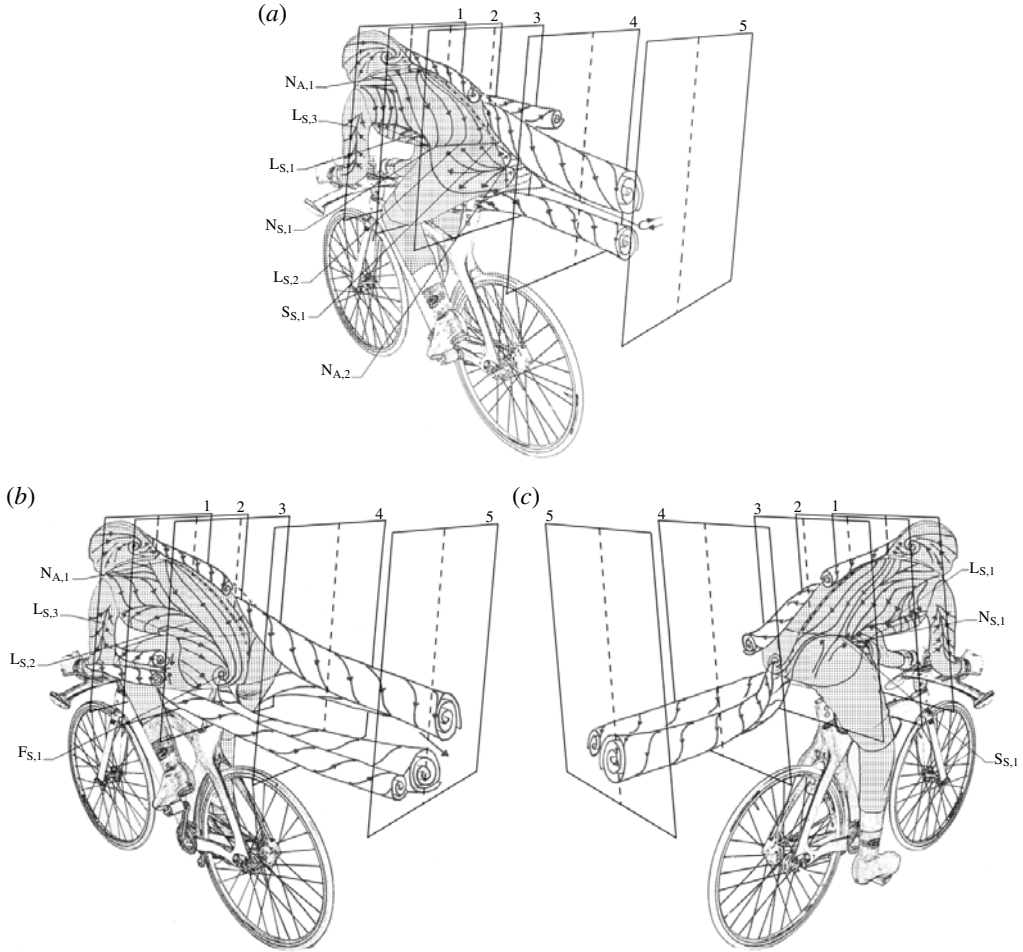


FIGURE 9. Flow topology of the streamwise vortex system for (a) 15° symmetrical low-drag flow regime and 75° asymmetrical high-drag flow regime viewed from (b) the left-hand side and (c) the right-hand side. Symbols L, N, S and F denote major lines, nodes, saddle points and foci, respectively, with subscript letters S and A indicating whether they are associated with separation or attachment. Subscript numbers are used to identify critical points when addressing results in support of the proposed skin friction patterns.

are identified and compared for each flow regime. The formation mechanisms of vortex structures are described using both the quantitative traverse results and the qualitative skin friction patterns. As the complete skin friction topology over the entire body of the mannequin was not investigated, the Poincaré–Bendixson theorem (hairy-sphere theorem) (Perry & Chong 1987), which stipulates that for an isolated three-dimensional body the number of nodes minus the number of saddles must equal two, does not apply to the back of the mannequin where skin friction flow visualizations were performed.

3.5.1. Comparison of low- and high-drag flow regimes

The additional streamwise traverses and skin friction flow visualizations performed for the 15 and 75° leg positions show an added complexity to the wake structure

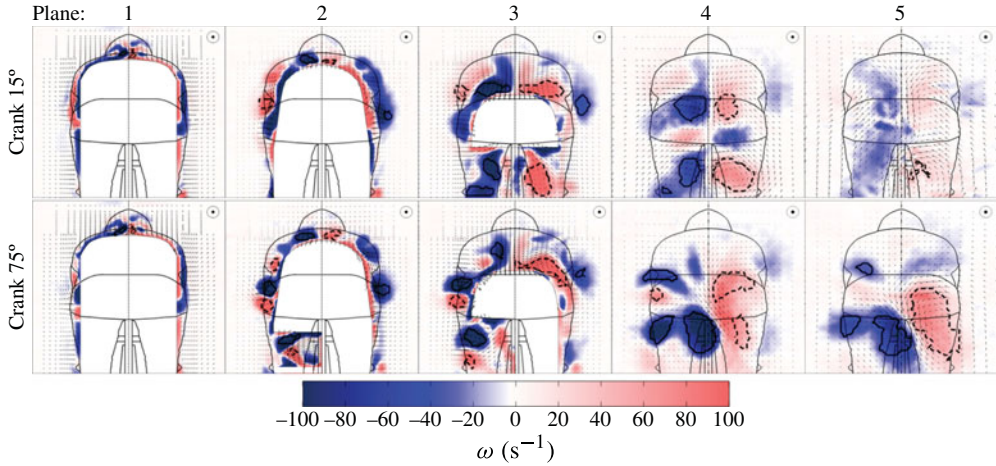


FIGURE 10. (Colour online) A comparison of contours streamwise vorticity for symmetrical and asymmetrical flow regimes at each streamwise traverse plane. Vortex boundaries identified using the swirling strength criterion have been outlined using solid and dashed lines. Solid lines outline vortex structures of clockwise rotation and dashed lines show vortices of anti-clockwise rotation.

to that previously described for the low- and high-drag flow regimes. As depicted in figure 9 multiple streamwise vortex structures, in addition to the primary vortices previously described in § 3.3, are identified as a key feature of the flow around cyclists. Even for the symmetrical low drag flow regime, traverse results reveal several areas on the body of the mannequin that provide a strong source of streamwise vorticity of similar magnitude to that of the high drag flow regime that is not captured in the previously analysed wake traverses (plane 5). Traverse results not only show the spatial development of the time-averaged flow over the body and into the near wake but also further highlight the significant differences in the low-drag (symmetrical) and high-drag (asymmetrical) flow regimes.

For the low-drag 15° leg position the body traverses show symmetry in the flow not only in the near wake but also over the entire upper body. This is in direct contrast to the 75° high-drag leg position where asymmetries in the near-wake flow can be seen to develop early over the body. This is shown in figure 10, which compares contours of the out-of-plane streamwise vorticity for both flow regimes. Clearly, the mechanisms by which the flow develops over the body of the mannequin and into the near wake is very different for each case.

The largest variations between the flow regimes shown in figure 10 arises from the difference in the streamwise vortices present in each of the planes, as identified using the swirling strength criterion previously discussed in § 3.3. These streamwise vortices have been visualized and are labelled in figures 11 and 12. Figure 11 compares isosurfaces of the primary vortices for each flow regime and figure 12 compares isosurfaces of the smaller secondary vortex structures that either merge with the primary vortices or decay by cross-diffusive annihilation close to the rear of the mannequin in the near wake. The origin of the major flow structures on the body of the mannequin in each flow regime is visualized in figures 13 and 14, which show images of skin friction flow visualizations for the low- and high-drag flow regimes, respectively.

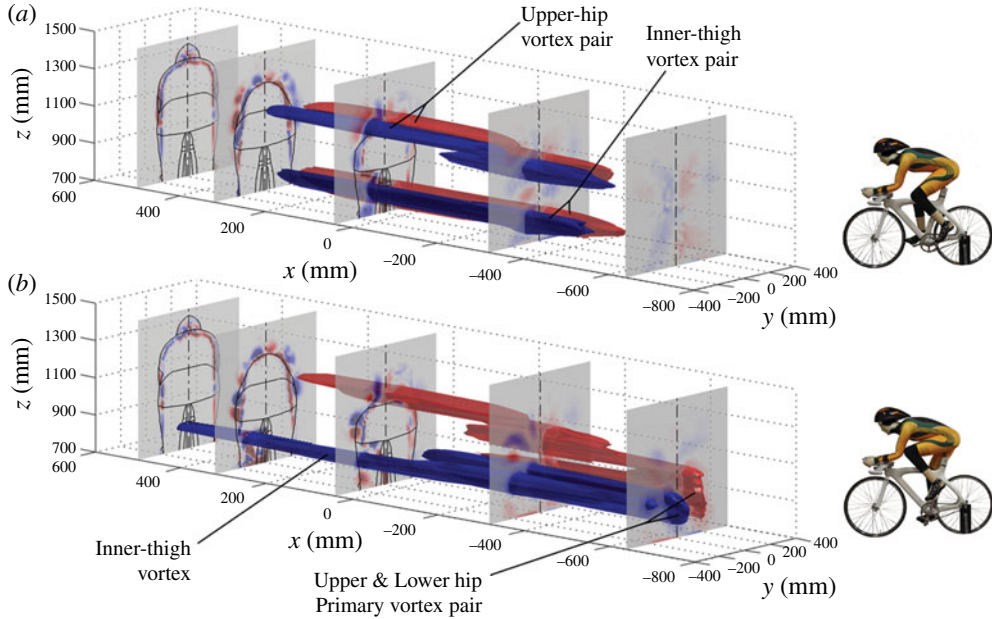


FIGURE 11. (Colour online) Spatial development of primary vortex structures over the body of the mannequin for (a) 15° symmetrical low-drag flow regime and (b) 75° asymmetrical high-drag flow regime. Dark (shown in blue online) and light (shown in red online) colours represent clockwise and anti-clockwise rotation, respectively.

For the 15° symmetrical low-drag flow regime in figure 11(a) a large vortex pair is seen to develop evenly over the upper hips on both sides of the body. This streamwise vortex pair is analogous to streamwise vortices that develop over low-aspect-ratio wings due to a pressure differential between the underside of the torso and the suction surfaces of the back. This pressure differential generates a strong flow that is directed up and around both sides of the torso and hips where flow separates and shear layers roll up from both sides of the body. This can be seen in figure 15 for the 15° leg position, which shows contour levels of the in-plane vertical component of velocity reaching 50% of the free-stream velocity around the sides of the torso, where this vortex pair starts to form at plane 2. Flow that is directed up around the sides of the torso and hips separates along the $(L_{S,1})$ separation line which has been visualized using the fluorescent oil and ink dot method in figure 13(a,d), respectively. The separated shear layers that roll up to form the upper-hip vortex pair which cover the entire span of the hips remain attached down the centreline of the back until they detach from the body at the separation saddle $(S_{S,1})$ shown in figure 13(b) and along the major separation line labelled $(L_{S,2})$. This separation line is also identified using the ink dot method where tracer dots finish in figure 13(d,e) due to the zero wall shear stress along lines of separation. As this vortex pair develops over the back figure 15 shows a strong down wash is generated in between them aiding in the attachment of the flow down the centreline of the back for the 15° leg position.

A second primary streamwise vortex pair can be seen between the upper legs below the hips in plane 3 of figure 10 for the symmetrical 15° flow regime. This vortex pair, of the same sign as the upper-hip vortex pair above, forms when flow separates along the inner thighs of both upper legs. With the upper legs aligned, the

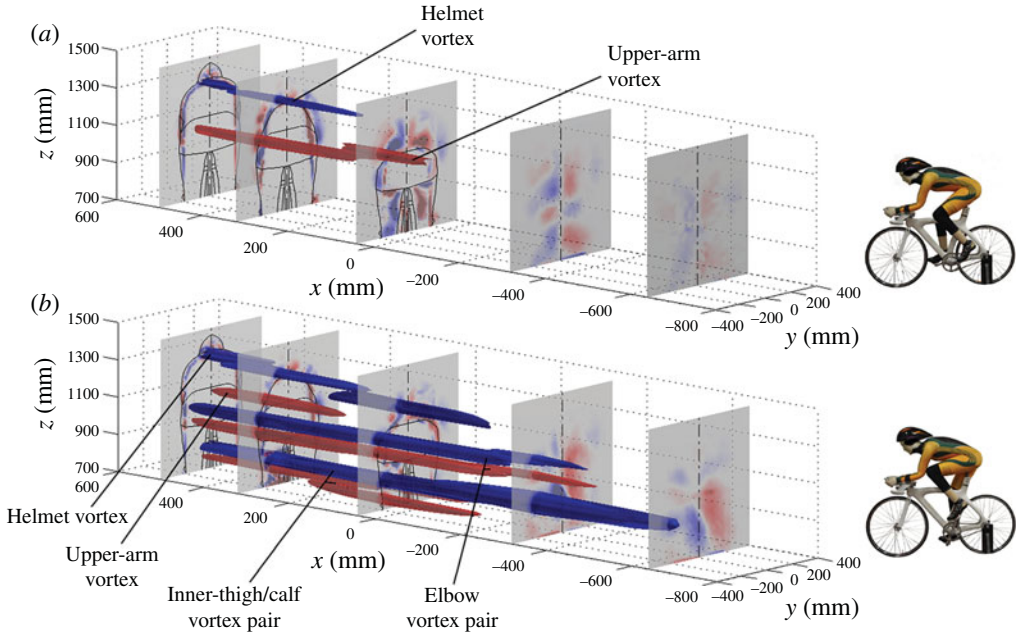


FIGURE 12. (Colour online) Spatial development of secondary vortex structures over the left-hand side of the mannequin for (a) 15° symmetrical low-drag flow regime and (b) 75° asymmetrical high-drag flow regime. Dark (shown in blue online) and light (shown in red online) colours represent clockwise and anti-clockwise rotation respectively. Secondary flow structures on the right hand side of the body for both flow regimes are characteristic of that shown for the symmetrical flow regime (a) (of opposite sign).

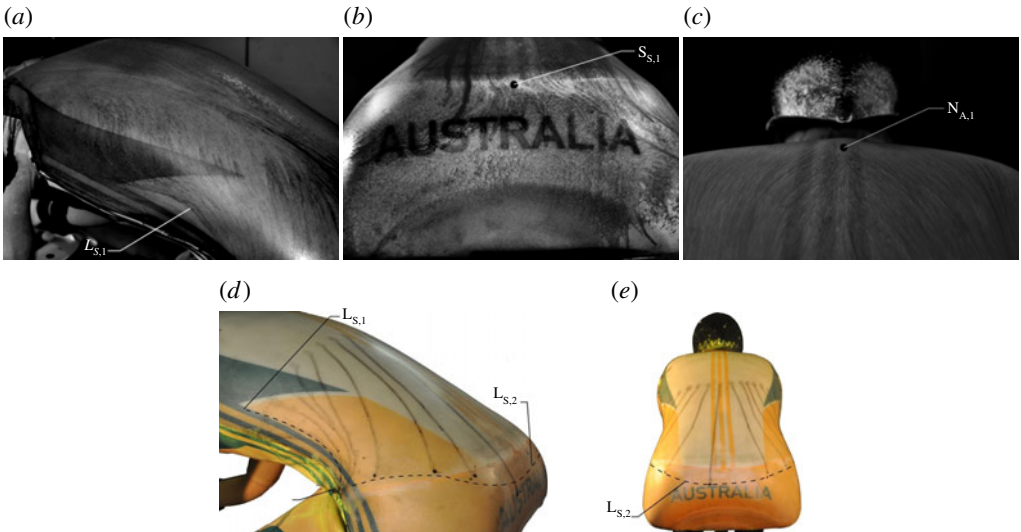


FIGURE 13. (Colour online) Skin friction flow patterns on the suction surface of the mannequin's back for the 15° symmetrical low-drag flow regime.

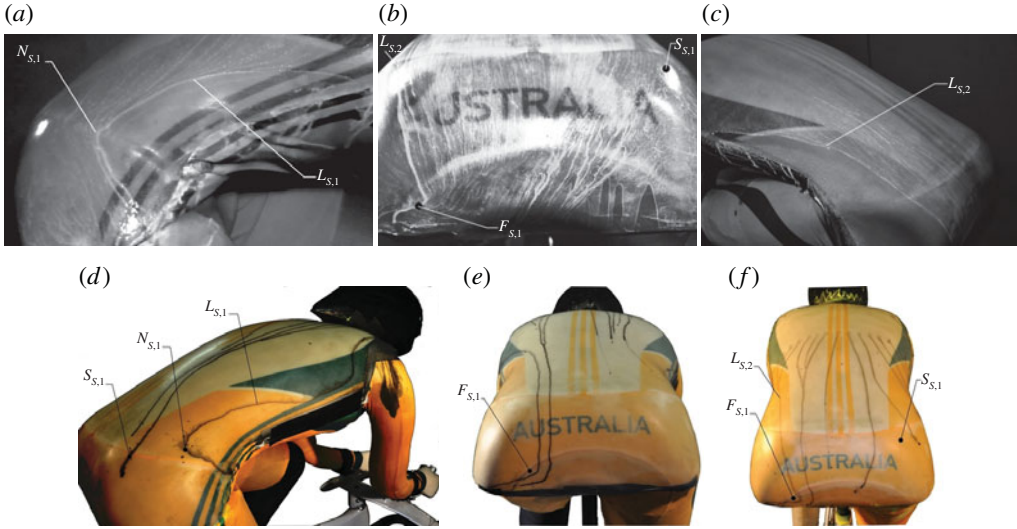


FIGURE 14. (Colour online) Skin friction flow patterns on the suction surface of the mannequin's back for the 75° asymmetrical high-drag flow regime.

strength of both vortex pairs are of similar magnitude. As these vortices leave the body of the mannequin they are drawn together in the near wake, which can be seen between planes 3 and 4 of figure 10. This forms a quadruple structure with upper- and lower-vortex pairs both exhibiting a downwash with a high-shear flow in between them. Between planes 4 and 5 we see a significant contraction in the wake as vortices of similar strength and opposite sign on either side of the centre line mutually interact. This results in the cross-annihilation of vorticity and the absence of coherent streamwise vortices a torso length behind the mannequin for the symmetrical leg positions.

For the 75° leg position, figure 11(b) shows where the primary vortex structures of the asymmetrical flow regime, which have previously been identified and analysed in §§ 3.3 and 3.4, originate and develop over the body of the mannequin. On the right side of the body for the 75° leg position where the hip angle is open, the upper-hip vortex develops in a manner comparable with that of the upper-hip vortices that span the lower back in the 15° leg position. The large streamwise vortex is clearly evident in plane three on the right-hand side of figure 10 for the 75° leg position. Although this is analogous to flow separation on the sides of the torso and hips for the low-drag case, flow separation along the primary ($L_{S,1}$) separation line occurs much higher on this side of the torso for the 75° leg position, as shown in figure 14(a). We also see that the vertical component of velocity on the sides of the torso where this structure develops is higher for the 75° leg position which reaches over 50% of the free-stream velocity as shown in plane 2 of figure 15 for the 75° leg position. Around the hip joint area a large 'kink' in this separation line can be seen which is associated with the node–saddle point combination of ($N_{S,1}$) and ($S_{S,1}$) shown in figure 14(b,d), which marks the location where the upper-hip vortex detaches from the lower back. As the upper-hip vortex advects downstream the time-averaged results show that it elongates. The near wake traverses indicate that this is a result of its merging with vorticity of the same sign that is fed into the wake behind the straightened upper leg. This

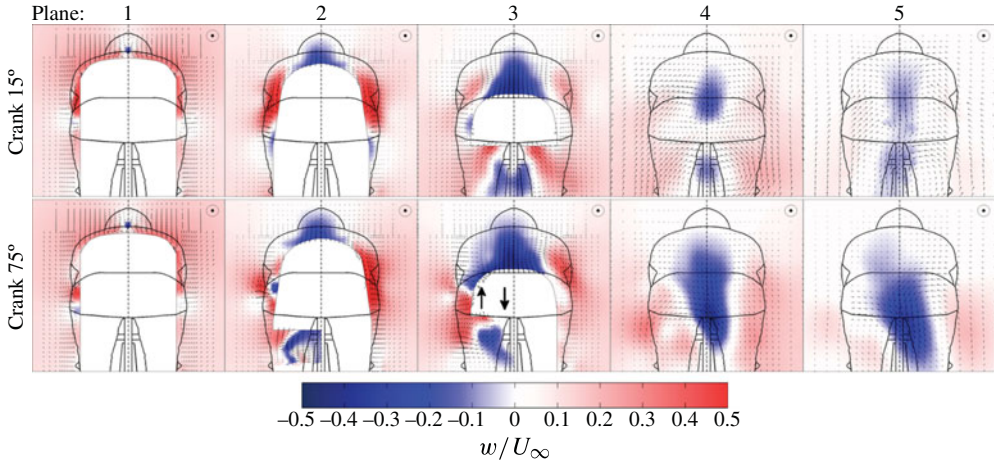


FIGURE 15. (Colour online) A comparison of contours of the vertical component of velocity for symmetrical and asymmetrical flow regimes at each streamwise traverse plane. Dark (shown in blue online) represents the downward direction and light (shown in red online) represents the upward direction.

elongated hip vortex is visualized further downstream in the isosurfaces shown in figure 11(b).

Although there are similarities in the development of the upper-hip vortices in both flow regimes, this is where the similarities between the two flow regimes end. With the hip angle closed the higher pressure flow from the underside of the torso is restricted from accelerating around its curved side. This results in the absence of the high vertical component of velocity on this side of the torso as shown in figure 15 on the left-hand side of plane 2 for the 75° leg position. Flow that is directed under the torso is split around the extended leg and either progresses up around the torso on this side of the body or out under the raised leg, where the flow separates from the inner thigh forming the inner-thigh vortex visualized in figure 11. The development of this structure is clearly captured under the raised leg in traverse plane 2 performed at the mid-torso chord. Unlike the development of the inner-thigh vortices of the symmetrical flow regime, this vortex develops further out from the centreline of the mannequin and develops in combination with a smaller secondary vortex that originates from the inner calf of the lower leg to form the counter rotating vortex pair (inner thigh/calf vortex pair) labelled in figure 12(b). This is a result of the strong flow component that is channelled out under the raised upper leg due to the high blockage arising from the straightened leg and the bicycle frame. This can be seen in plane 2 of figure 16 for the 75° leg position which shows a large horizontal component of velocity of up to 50% of the free-stream velocity that is being directed away from the straightened leg out underneath the raised leg. Compared with the 15° symmetrical flow regime this results in a large low-velocity recirculation region between the legs below the hips that extends out from the straightened leg. This is evident in plane 3 of figure 17 which compare contours of the non-dimensional free-stream velocity for both leg positions and further illustrates differences between the two flow regimes.

The restriction imposed by the raised leg not only impacts the flow directed under the torso but all around it. Flow that is directed around the raised leg and torso does

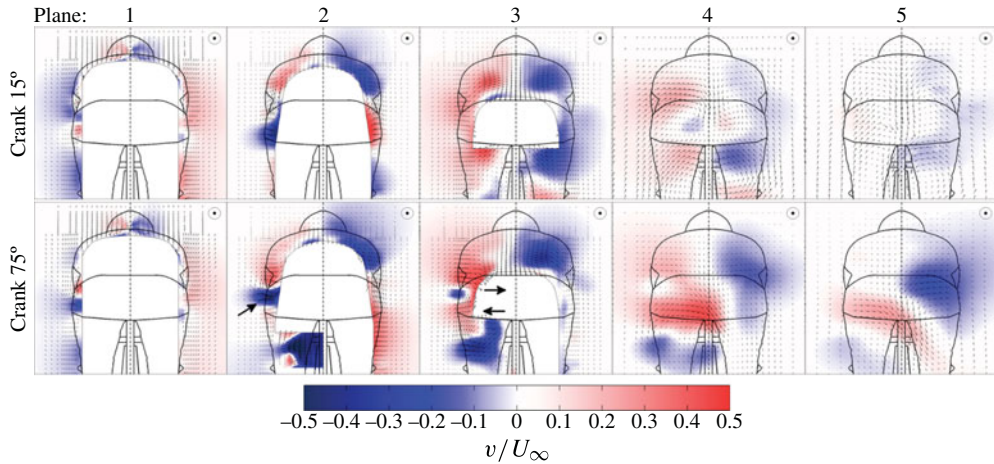


FIGURE 16. (Colour online) A comparison of contours of spanwise velocity for symmetrical and asymmetrical flow regimes at each streamwise traverse plane. Dark (shown in blue online) represents the left spanwise direction and light (shown in red online) represents the right spanwise direction.

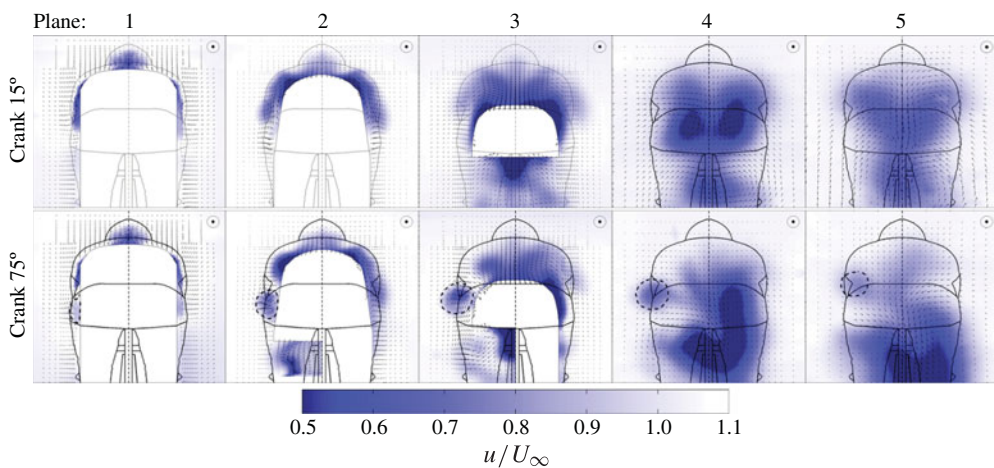


FIGURE 17. (Colour online) A comparison of contours of streamwise velocity for symmetrical and asymmetrical flow regimes at each streamwise traverse plane. Dashed lines highlight isolated section of the wake that develops downstream of the arm/elbow joint.

not see the full extent of the curvature of the upper leg (which is primarily aligned with the free stream in this position) and the torso sides, remaining largely attached over the side of the torso where it separates along the separation line labelled ($L_{S,2}$) in figure 14(c). This separation line begins at the armpit junction and extends the entire length of the back over the upper and lower hip. Below this separation line the oil flow visualization of figure 14(c) shows a turbulent boundary layer where the high momentum flow near the body surface not only aids in the attachment of the flow around the hip, but also increases the flow rate of the oil fluid in this region, leaving behind a textured pattern that is largely devoid of the fluorescent powder.

As the flow progresses around the torso and under the raised leg the mean velocity vectors show the flow spiralling around the rear of the hip of the raised leg. This is demonstrated with arrows which have been drawn on the left hip of figures 15 and 16 showing the circulatory motion of the in-plane velocity components around the raised hip. Skin friction streamlines on the rear of the raised hip shown in figure 14(b) can also be seen to spiral around the marked focus ($F_{S,1}$). This marks the origin of the lower-hip vortex. Further evidence of this surface flow topology is provided by the localized surface streamlines using the ink dot method shown in figure 14(e,f), where in the vicinity of the focus ($F_{S,1}$) we see a severe deviation in these lines around the focal point. We also see the focus ($F_{S,1}$), which forms in combination with the separation saddle ($S_{S,1}$), marking the termination point of the separation line ($L_{S,2}$). The three-dimensional focus on the lower hip accounts for the sudden increase in vorticity below the hips between planes 3 and 4 in figure 10 for the 75° leg position, as a result of the formation the lower-hip vortex between these planes.

The formation and development of secondary streamwise vortices that originate upstream of the primary structures is also dependent on the position of the legs. This is clearly shown in the isosurfaces of these structures shown in figure 12, that show large variations in streamwise vortices that originate on the left-hand side of the mannequin from the helmet, arms and legs for the 15 and 75° leg positions. For both leg positions contours of streamwise vorticity in the plane at the trailing edge of the helmet show a streamwise vortex pair that originates when shear layers roll up from both sides of the helmet. This has been shown to be a characteristic feature of the flow behind helmets by Chabroux *et al.* (2010) who performed similar wake surveys behind different helmets using particle image velocimetry. Downstream of the tip of the helmet the flow reattaches to the body which is marked by an attachment node ($N_{A,1}$) shown in figure 13(c). For the 15° leg position the helmet vortices remain attached down the back where they merge downstream with the primary upper-hip streamwise vortices which are of the same sign. For the asymmetrical flow regime vortices that originate from the helmet on the side of the body were a upper-hip vortex does not form (side where leg is raised), persist much further into the near wake behind the mannequin which is evident for the 75° position in figure 12(b).

With the hip angle closed, the wake from the arms on the side of the body with the leg in a raised position can develop downstream over the body of the mannequin. This is shown in figure 12(b) where multiple streamwise vortices are identified in the wake of the arms, as opposed to the 15° leg position figure 12(a) (and the right-hand side of the 75° leg position). On this side of the body the wake flow behind the arms is dominated by the turbulent flow driven up the sides of the torso by the large pressure differential between the underside of the torso and back. A streamwise vortex can be seen in both flow regimes to develop when flow separates from the outside of the upper arm of the mannequin. This generates vorticity that is advected up towards the shoulder due to a strong component of the flow that is directed up the arm. Flow separation from the arms has been visualized by Brownlie *et al.* (2009) using a similar fluorescent China clay technique performed on a mannequin in a time trail position which clearly identifies the major upper-arm separation line marked by ($L_{S,3}$) in figure 9.

Around the armpit junction the separated shear layers from the upper arm are turned and advected downstream by the mean flow resulting in the upper-arm vortex. The trajectory of this vortex over the back is similar to that of the separation line ($L_{S,2}$) that originates behind the armpit on the side of the torso, identified in figure 13(b) from the oil flow visualizations. Owing the sign and the close proximity of this streamwise

vortex to the body of the mannequin, it has the effect of ‘lifting’ the flow from the surface of the model, aiding in flow separating from this side of the torso along the separation line ($L_{S,2}$).

A strong streamwise vortex pair that can also be seen to develop behind the left elbow joint in plane 1 and is clearly identified in planes 2–4 of figure 10 for the 75° leg position. This vortex pair is labelled the ‘elbow vortex pair’ in the isosurface of the secondary structures shown in figure 12(b). As this vortex pair is advected down along the side of the torso we see that a strong horizontal jet is generated outwards from the side of the torso in between the vortex pair. This is highlighted by the arrow drawn in the contours of the spanwise component of velocity in plane 2 of figure 16 for the 75° leg position. In tracing the trajectory of this vortex pair from the elbow joint into the near wake we see that it is responsible for the isolated turbulent velocity deficit region described previously in § 3.2 that discusses the time-averaged wake profiles for the varying leg positions around the crank cycle. This is further emphasized in the contour plots of streamwise velocity by the dashed circles that isolate the velocity defect regions associated with the elbow vortex pair in planes 1–5 of figure 17. The highlighted regions show that the elbow–vortex pair follows an upwards trajectory into the wake behind the mannequin.

3.6. Effect of crank angle on surface pressures

Having identified the primary flow structures and flow regimes that develop throughout the crank cycle, we now turn our attention to the direct impact that they have on surface pressures. Figure 18 shows contours of the time-averaged surface pressure coefficient on the suction surface of the mannequin’s back for selected leg positions in the first half of the crank cycle. Surface pressure measurements clearly show that leg position has a dramatic effect on both the magnitude and distribution of these pressures throughout the crank cycle. Please also see the supplementary movies available at <http://dx.doi.org/10.1017/jfm.2013.678>.

During the symmetrical flow regime, 0 and 15° leg positions display a characteristic symmetrical high pressure recovery distribution. The presences of the low-pressure hip vortices on the sides of the torso are apparent. Where the flow separates across the back of the hips ($L_{S,2}$ symmetrical flow regime), we see a slight reduction in surface pressure followed by a significant increase, with the surface pressure peaking in the middle of the lower back. This is consistent with a small recirculation region that is characterized by a small spanwise counter rotating vortex pair that is fed by the flow coming off the back and up from beneath the upper legs, below the base of the hips. This results in the reattachment of the flow to the base of the mannequin that is marked by an attachment node ($N_{A,2}$). This is demonstrated in the proposed skin friction lines that have been overlayed on the contours of the surface pressure coefficient for the 15° leg position.

As the legs progress around the crank cycle we see the surface pressure distribution become increasingly more asymmetrical with significant pressure gradients. As the flow transitions to the asymmetrical flow regime large low-pressure regions develop where the primary upper- and lower-hip vortex pair originate. This is clearly shown for the 75° leg position in figure 18 which also shows the skin friction flow topology for the asymmetrical flow regime overlayed on the surface pressure contours.

Low-pressure regions attributed to the primary vortex pair in the asymmetrical flow regime result in the majority of the variation in drag throughout the crank cycle. Figure 19 compares the suction drag on the back of the mannequin with

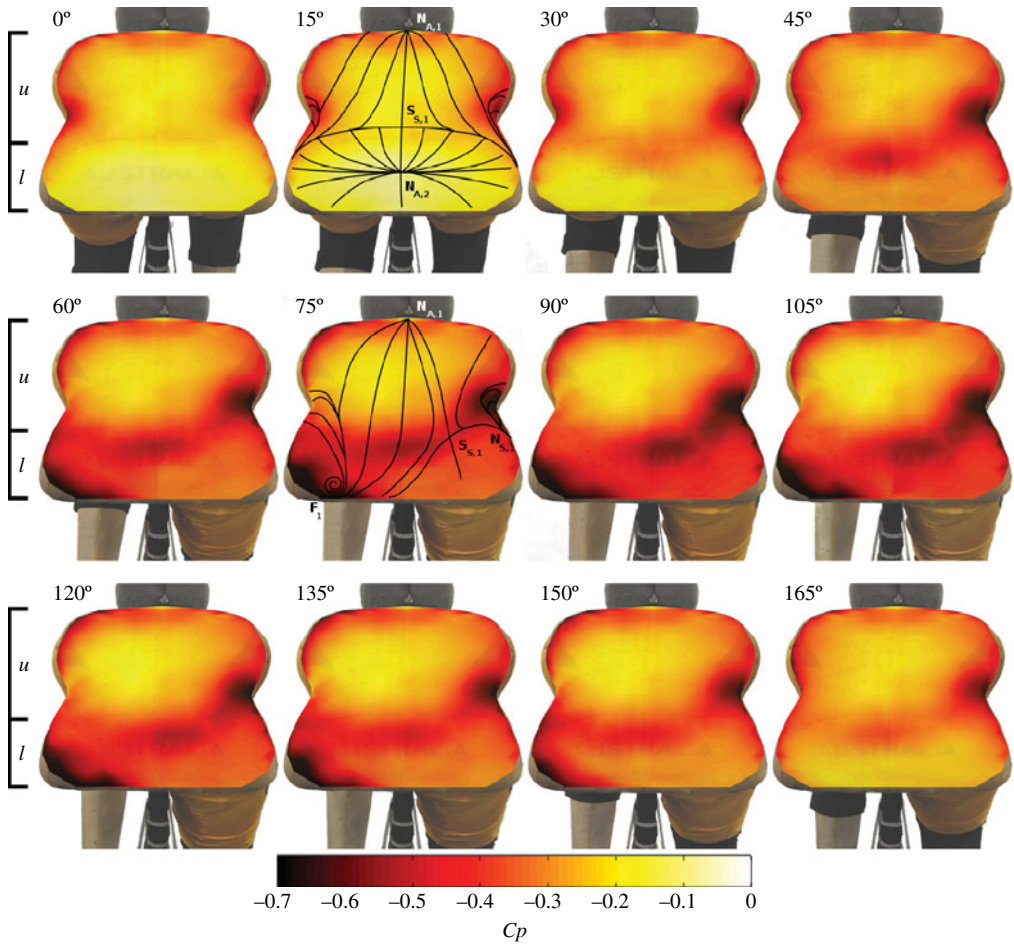


FIGURE 18. (Colour online) Surface pressure distributions showing the development of surface pressures throughout the first half of the crank cycle.

the drag measured using the Kistler force balance. The suction drag $C_D A C_p$ on the back has been calculated by integrating the surface pressure coefficient over the area of the mannequin's back that is normal to the free-stream direction. The relative contributions of upper- and lower-back regions, which contain the formation region of each of the primary vortices, to the total back suction drag is also shown where the upper and lower sections of the back have been marked in figure 18 with 'u' and 'l', respectively. Although the suction drag from the back only accounts for 12–20% of the total drag throughout the crank cycle, it accounts for more than 60% of the variation in drag between the low- and high-drag leg positions. As a result of the lower back surfaces where the lower-hip vortex originates being primarily aligned with the drag producing direction, more than 75% of the variation in the back suction drag is a result of the surface pressures acting on the lower back.

4. Conclusions

Findings highlight the fact that the optimization of cycling aerodynamics cannot be assessed from the projected frontal area of cyclists alone, and show that the

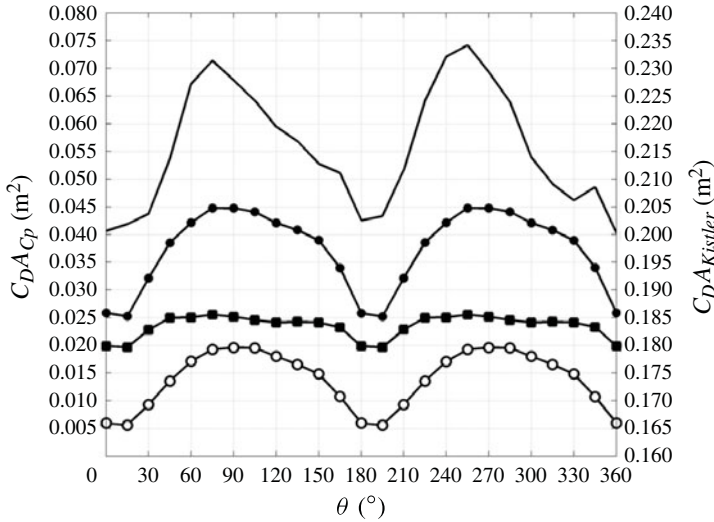


FIGURE 19. Left-hand axis: Suction drag as a function of crank angle from back total (—●—), upper back (—■—) and lower back (—○—). Right-hand axis: Drag measured by Kistler force balance (—). Note that both axes are of the same scale.

variation in drag measured throughout a crank cycle is better explained through the effect that leg position has on large-scale flow structures. For flows around cyclist geometries, typical of elite athletes in a time trial position, the primary features of the flow structure consist of a large trailing streamwise vortex system. Changes in the large-scale flow structures are the primary mechanisms effecting the large variation in the drag measured throughout the crank cycle. The formation, strength and interaction of primary vortex structures is dependent on leg position. This results in large variations in the pressure distribution acting on the suction surfaces of the back where these structures originate and consequently also on the drag force which is mainly a result of the pressure drag.

Two characteristic low- and high-drag flow regimes were found to account for the main variations in the structure and topology of the flow throughout the crank cycle and show that multiple flow regimes must be considered when optimizing the aerodynamics of cyclists. The primary feature of the low-drag flow regime consists of streamwise vortices that originate from the upper and inner thighs forming a quadrupole arrangement of similar sign vortex pairs orientated symmetrically in the centre plane of the mannequin. The symmetrical regime results in a beneficial contraction of the near wake due to the mutual interaction of similar strength vortices. For the high-drag flow regime the large-scale flow structures consist of streamwise vortices that originate when flow separates from the upper hip of extended leg and the rear of the hip of the raised leg. The upper- and lower-hip vortex pair is orientated asymmetrically in the centre plane and persists much further into the wake flow compared to the primary vortices of the symmetrical low-drag flow regime.

Although there are many factors that affect the aerodynamics of cyclists, a deeper understanding of how complex bluff-body cyclist geometries influence aerodynamic drag now exists, resulting in drastic potential for performance improvements. Currently the impact of rider geometry, position and equipment on the large-scale flow structures is unknown, a fact that is reflected in the current trial and error approach to optimizing

rider aerodynamics. With an understanding of the individual large-scale flow structures a solid foundation is formed for addressing this shortfall in our application of cycling aerodynamics. With numerical codes becoming increasingly important in the design of cycling equipment and the optimization of cyclist aerodynamics, an understanding of the large-scale structures will aid in the interpretation and validation of numerical results. The high dependence of the drag on the development and strength of primary vortices suggests that there is a great potential to improve rider aerodynamics through a targeted approach at reducing the drag associated with these flow structures.

Supplementary movies

Supplementary movies are available at <http://dx.doi.org/10.1017/jfm.2013.678>.

REFERENCES

- BROWNLIE, L., KYLE, C., CARBO, J., DEMAREST, N., HARBER, E., MACDONALD, R. & NORDSTROM, M. 2009 Streamlining the time trial apparel of cyclists: the Nike Swift Spin project. *Sports Technol.* **2** (1–2), 53–60.
- CARMER, C. F. V., KONRATH, R., SCHRÖDER, A. & MONNIER, J.-C. 2008 Identification of vortex pairs in aircraft wakes from sectional velocity data. *Exp. Fluids* **44** (3), 367–380.
- CHABROUX, V., MBA, M. N., SAINTON, P. & FAVIER, D. 2010 Wake characteristics of time trial helmets using PIV-3C technique. In *15th Int. Symp. on Applications of Laser Techniques to Fluid Mechanics, Lisbon, Portugal, 5–8 July 2010*, Available at: http://ltes.dem.ist.utl.pt/lxaser/lxaser2010/upload/1586_lfpkgn_4.1.3.Full_1586.pdf.
- HOOPER, J. D. & MUSGROVE, A. R. 1997 Reynolds stress, mean velocity, and dynamic static pressure measurement by a four-hole pressure probe. *Exp. Thermal Fluid Sci.* **15** (4), 375–383.
- HORNUNG, H. & PERRY, A. E. 1984 Some aspects of three-dimensional separation. I—Streamsurface bifurcations. *Z. Flugw. Welt.* **8**, 77–87.
- HUCHO, W. & SOVRAN, G. 1993 Aerodynamics of road vehicles. *Annu. Rev. Fluid Mech.* **25** (1), 485–537.
- KYLE, C. R. & BURKE, E. R. 1984 Improving the racing bicycle. *Mech. Engng* **106** (9), 34–45.
- LANGSTON, L. S. & BOYLE, M. T. 1982 A new surface-streamline flow-visualization technique. *J. Fluid Mech.* **125** (1), 53–57.
- LUKES, R. A., CHIN, S. B. & HAAKE, S. J. 2005 The understanding and development of cycling aerodynamics. *Sports Engng* **8** (2), 59–74.
- MALTBY, R. L. 1962 Flow visualization in wind tunnels using indicators. Tech. Rep. DTIC Document.
- MARTIN, J. C., DAVIDSON, C. J. & PARDYJAK, E. R. 2007 Understanding sprint-cycling performance: the integration of muscle power, resistance, and modeling. *Intl J. Sports Physiol. Perform.* **2** (1), 5.
- MARTIN, J. C., MILLIKEN, D. L., COBB, J. E., MCFADDEN, K. L. & COGGAN, A. R. 1998 Validation of a mathematical model for road cycling power. *J. Appl. Biomech.* **14**, 276–291.
- MASKELL, E. C. 1963 A theory of the blockage effects on bluff bodies and stalled wings in a closed wind tunnel. Tech. Rep. DTIC Document.
- MASKELL, E. C. 1973 Progress Towards a Method for the Measurement of the Components of the Drag of a Wing of Finite Span. Procurement Executive, Ministry of Defence.
- MERCKER, E. & WIEDEMANN, J. 1996 On the correction of interference effects in open jet wind tunnels. *SAE Trans. J. Engines* **105** (6), 795–809.
- PEAKE, D. J. & TOBAK, M. 1982 Three-dimensional separation and reattachment. DTIC Document 84221.
- PERRY, A. E. & CHONG, M. S. 1987 A description of eddying motions and flow patterns using critical-point concepts. *Annu. Rev. Fluid Mech.* **19** (1), 125–155.
- RAMBERG, S. E. 1983 The effects of yaw and finite length upon the vortex wakes of stationary and vibrating circular cylinders. *J. Fluid Mech.* **128** (1), 81–107.

- SHEPHERD, I. C. 1981 A four hole pressure probe for fluid flow measurements in three dimensions. *J. Fluids Engng* **103**, 590–594.
- CAMERON, T., YARIN, A. & FOSS, J. F. (Eds) 2007 *Springer Handbook of Experimental Fluid Mechanics*. vol. 1. Springer.
- ZDRAVKOVICH, M. M., ASHCROFT, M. W., CHISHOLM, S. J. & HICKS, N. 1996 Effect of cyclists' posture and vicinity of another cyclists on aerodynamic drag. *Engng Sport* **1**, 21–28.
- ZHOU, J., ADRIAN, R. J., BALACHANDAR, S. & KENDALL, T. M. 1999 Mechanisms for generating coherent packets of hairpin vortices in channel flow. *J. Fluid Mech.* **387** (1), 353–396.